Efficient time splitting schemes for the monodomain equation in cardiac electrophysiology

Laura P. Lindner, Tobias Gerach, Tobias Jahnke, Axel Loewe, Daniel Weiss, Christian Wieners

KARLSRUHE INSTITUTE OF TECHNOLOGY

CRC 1173

WaVe
phenomena

Participating universities

Universität Stuttgart

EBERHARD KARLS
UNIVERSITÄT
TÜBINGEN

TU
WIEN

Funded by

DFG

Efficient time splitting schemes for the monodomain equation in cardiac electrophysiology

Laura P. Lindner[1] | Tobias Gerach[2] | Tobias Jahnke[1] | Axel Loewe[2] | Daniel Weiss[1] |
Christian Wieners[1]

[1]Institute of Applied and Numerical
 Mathematics, Karlsruhe Institute of
 Technology (KIT), Karlsruhe, Germany
[2]Institute of Biomedical Engineering,
 Karlsruhe Institute of Technology (KIT),
 Karlsruhe, Germany

Correspondence
Christian Wieners
Email: christian.wieners@kit.edu

Summary

Approximating the fast dynamics of depolarization waves in the human heart described by the monodomain model is numerically challenging. Splitting methods for the PDE-ODE coupling enable the computation with very fine space and time discretizations. Here, we compare different splitting approaches regarding convergence, accuracy and efficiency. Simulations were performed for a benchmark configuration with the Beeler–Reuter cell model on a truncated ellipsoid approximating the left ventricle including a localized stimulation. For this benchmark configuration, we provide a reference solution for the transmembrane potential. We found a semi-implicit approach with state variable interpolation to be the most efficient scheme. The results are transferred to a more physiological setup using a bi-ventricular domain with a complex external stimulation pattern to evaluate the accuracy of the activation time for different resolutions in space and time.

KEYWORDS:

cardiac electrophysiology, monodomain equation, Beeler–Reuter cell model, splitting methods, time integration

1 | INTRODUCTION

To replicate the human heart's function numerically, the efficient approximation of the electrophysiology plays a key role, since the overall cardiac mechanisms are controlled by the propagation of the depolarization waves and the chemical reactions which are initiated by the electric stimulus. This process is described by the physiology-based bidomain equations consisting of two partial differential equations (PDEs) for modeling the intra- and extracellular potentials. The PDEs are coupled with a system of ordinary differential equations (ODEs) for the cellular model describing the ion currents across the membrane. A detailed derivation of the bidomain model is given by Franzone and Savaré [1]. Assuming that the anisotropic intra- and extracellular conductivities are proportional to each other, results in the simpler monodomain model, a parabolic PDE describing the transmembrane voltage v, the difference of the intra- and extracellular potentials. This simpler model is computationally less demanding but still reproduces the main phenomena of wave propagation in the heart, see, e.g., Bourgault and Pierre [2].

A major computational challenge for the monodomain model is the large range of time scales varying from about a second for the heart beat to a nearly instantaneous response of the gating mechanisms (few microseconds). Since for realistic cell models a fully implicit scheme in time is prohibitively expensive due to the large number of unknowns, the standard approach is to use a splitting method for the time integration of the coupled PDE-ODE system. This means that in each time step, the ODEs describing the gating mechanisms, the ODEs for the evolution of the intracellular ion concentrations and the parabolic PDE for the transmembrane voltage are propagated successively. We denote this approach as component-wise splitting. Commonly,

an additional operator spitting of the PDE into the reaction and the diffusion part is used. Schemes based on the reaction-diffusion splitting are for example the first-order Godunov method [3] or the second-order Strang splitting [4]. Because of the very fast dynamics of the gating mechanisms, the operator splitting approach is often combined with the observation of Rush and Larson [5] that the (linear) ODEs describing the gating variables can be solved exactly as long as the transmembrane voltage is kept fixed. This idea can also be used for the component-wise splitting approach.

As there is no analytical solution of the monodomain problem, the accuracy of time integration approaches has to be studied numerically. For example Sundnes et al. [3] confirmed the convergence behavior of several operator splitting methods combined with the simple FitzHugh–Nagumo model for a 1d domain. The depedency of the conduction velocity on the spatial resolution was reported in several studies [6, 7]. Niederer et al. [8] defined a benchmark setup on a 3d cuboid and studied the approximations of the activation time on 11 different platforms for cardiac simulations. More recently, the convergence and accuracy of time integrators where studied on 1d and 2d regular rectangular domains with simplified external stimulus, for example by Roy et al. [9] and Woodworth et al. [10]. But as Krishnamoorthi et al. [11] already observed, the irregularity of the mesh has an immense impact on physiological properties. As realistic heart simulations are performed on non-uniform meshes, it is essential to test the behavior of commonly used time integration approaches systematically for more complex and anatomically more relevant scenarios.

Here, we define an electrophysiology benchmark on a truncated ellipsoid approximating the left ventricle, similar to the elasticity benchmark of Land et al. [12]. For this more realistic configuration, we investigate splitting schemes in time systematically by comparing different approaches in terms of stability and accuracy. The latter is done by means of a reference solution computed on a very fine mesh and with a very small time step. Furthermore, we evaluate computational efficiency. This extends results for the Godunov splitting as well as implicit methods discretizing the parabolic PDE for the transmembrane voltage [13, 14].

Our study includes the schemes from Pathmanathan et al. [15], where two approaches for approximating the total ionic current are compared: the ionic current interpolation (ICI) and state variable interpolation (SVI), both using semi-implicit time integration for a component-wise splitting ansatz. The ICI approach is a Lagrange interpolation of the total ionic current, while the SVI approach corresponds to the approximation of the L_2 projection. In numerical tests in [15], the difference of the approximation variants was elaborated, especially for coarse mesh resolutions. This work was extended in [11] by representing the state variables of the cell model at the quadrature points. They evaluated different lumping variants and the effect of the mesh size on physiological properties such as the conduction velocity of the depolarization wave. We confirm the difference of the approximations by ICI and SVI on the anatomically relevant electrophysiology benchmark setup, and we extend the investigation to a full time and space convergence study. We show that the reaction-diffusion splitting has the same numerical behavior as the ICI ansatz as it was supposed in [15]. Furthermore, we show that a component-wise splitting method with SVI is more efficient than the reaction-diffusion splitting or component-wise splitting combined with ICI. A main observation is that the stability of component-wise splitting is considerably improved by replacing the Lagrange interpolation in the PDE-ODE coupling by the L_2 projection. The smoothness of the external current in space and time has a strong influence on the convergence properties for solutions of the transmembrane voltage, thus the stimulus current requires suitable regularization. The results from the benchmark configuration are extended to a realistic bi-ventricular setting, where we investigate the convergence in space and time as well as the accuracy of the activation times using the semi-implicit scheme proposed in [14]. In space, we use linear conforming approximations, which is the standard approach. Nevertheless, a multitude of space discretizations has been studied, for example higher order elements [16, 17], isoparametric finite elements [18, 11], adaptive methods [19, 20] and non-conforming elements [21]. Our results complement these contributions by a comparison of time discretizations.

For this study, we restrict ourselves to the monodomain equation coupled with the Beeler–Reuter cell model [22] describing the evolution of the calcium ion concentration and six gating variables. This cell model is well established and includes the characteristic properties (including fast gating kinetics) which make the design of efficient and stable schemes challenging. For the numerical computation, we use the parallel finite element system M++ [23], which allows for very fine resolutions in space and time in order to obtain a reliable reference solution; this is required for the evaluation of the accuracy of the different time stepping schemes.

The paper is organized as follows: First, we introduce the monodomain equation and the Beeler–Reuter model in detail, and we summarize known existence and uniqueness as well as convergence results. Different numerical approximation schemes of the coupled PDE-ODE system in space and in time are described in the third section. In Sec. 4, we define a benchmark configuration on a truncated ellipsoid, provide a reference solution and study the convergence behavior and accuracy of different splitting approaches. In addition, we extend the investigation to a more realistic bi-ventricular domain. Finally, we conclude with a summary and an outlook on possible extensions of our results.

2 | THE MONODOMAIN EQUATION IN ELECTROPHYSIOLOGY

Modeling the electrophysiology in the human heart by the bidomain equation comprises the evolution of the extra-cellular and intra-cellular electric potentials, the concentration of several ions as well as the switching of gating variables which control the transport of ions across the membranes, cf. Vigmond et al. [24]. In our convergence study of time integration schemes, we consider a model which combines the monodomain equation for the transmembrane voltage (the difference of the extra-cellular and intra-cellular electric potentials) with a representative cell model introduced by Beeler and Reuter [22].

Let $\Omega \subset \mathbb{R}^3$ be a bounded Lipschitz domain and let $[0, T]$ be a time interval. The model describes the evolution of the transmembrane voltage v, the intra-cellular calcium ion concentration c, and the vector of six gating variables $\mathbf{w}$, solving the coupled PDE-ODE system

$$\chi C_{\mathrm{m}} \partial_t v - \nabla \cdot (\mathbf{D} \nabla v) + \chi I_{\mathrm{ion}}(v, c, \mathbf{w}) = \chi I_{\mathrm{ext}}, \tag{1a}$$

$$\partial_t c - G_c(v, c, \mathbf{w}) = 0, \tag{1b}$$

$$\partial_t \mathbf{w} - \mathbf{G_w}(v, \mathbf{w}) = \mathbf{0} \tag{1c}$$

in $[0, T] \times \Omega$ subject to the initial values

$$v(0, \mathbf{x}) = v^0(\mathbf{x}), \qquad c(0, \mathbf{x}) = c^0(\mathbf{x}), \qquad \mathbf{w}(0, \mathbf{x}) = \mathbf{w}^0(\mathbf{x}), \qquad \mathbf{x} \in \overline{\Omega} = \Omega \cup \partial\Omega \tag{1d}$$

at $t = 0$ and homogeneous Neumann boundary conditions

$$\mathbf{D} \nabla v \cdot \mathbf{n} = 0 \qquad \text{on } (0, T) \times \partial\Omega. \tag{1e}$$

Parameters of the monodomain model are the surface-to-volume ratio $\chi \in \mathbb{R}_+$, the membrane capacitance $C_{\mathrm{m}} \in \mathbb{R}_+$, and the conductivity tensor $\mathbf{D} : \overline{\Omega} \to \mathbb{R}^{3 \times 3}$ depending on the anisotropic cell structure, where we assume that the conductivity tensor $\mathbf{D}$ is symmetric, bounded and uniformly positive definite. For the Beeler–Reuter cell model, the total ionic current in (1a) is of the form

$$I_{\mathrm{ion}}(v, c, \mathbf{w}) = I_s(v, c, w_1, w_2) + I_{\mathrm{Na}}(v, w_3, w_4, w_5) + I_{x_1}(v, w_6) + I_{\mathrm{K}}(v), \tag{2}$$

depending polynomially on the gating variables $\mathbf{w}$, continuously on the electric voltage v, and logarithmically on the concentration c. The evolution is driven by the pacing from the cardiac conduction system comprising among other the sinus node in the atria and the Purkinje fibers in the ventricles. This is modeled by an external stimulus

$$I_{\mathrm{ext}} : [0, T] \times \overline{\Omega} \to \mathbb{R}, \qquad I_{\mathrm{ext}}(t, \mathbf{x}) = \begin{cases} a_i(t, \mathbf{x}) & \text{for } t \in [t_{\mathrm{beg},i}, t_{\mathrm{beg},i} + \tau_i], \ \mathbf{x} \in \overline{\Omega}_{\mathrm{stim},i}, \\ 0 & \text{else} \end{cases} \tag{3}$$

in the stimulation area $\overline{\Omega}_{\mathrm{stim}} = \bigcup_{i=1,\dots,n_{\mathrm{stim}}} \overline{\Omega}_{\mathrm{stim},i} \subset \overline{\Omega}$. Here, $\Omega_{\mathrm{stim},i}$ are disjoint sets, a_i are amplitude functions, $t_{\mathrm{beg},i} \in [0, T - \tau_i]$ is the starting time of the i-th stimulus and $\tau_i > 0$ is its duration ($i = 1, \dots, n_{\mathrm{stim}}$). In many applications the amplitude functions of the external stimulus I_{ext} are chosen to be constant functions, i.e., $a_i(t, \mathbf{x}) = a_i > 0$ in (3); cf. [14, 10, 7]. In this case, however, the function I_{ext} is discontinuous both in time and space, and the missing regularity has the effect that convergence of the numerical methods can only be observed for very fine discretizations. This is not appropriate for the numerical convergence study of the different time stepping schemes in Sec. 4. In our simulations, therefore, we use amplitudes for the external current I_{ext} of the form $a_i(t, \mathbf{x}) = a_{t,i}(t) a_{\mathbf{x},i}(\mathbf{x}) a_i$, $i = 1, \dots, n_{\mathrm{stim}}$, with $a_i > 0$ and

$$a_{t,i}(t) = \frac{1}{\pi} \Big(\arctan \big(s_{\mathrm{ext}}(t - t_{\mathrm{beg},i}) \big) - \arctan \big(s_{\mathrm{ext}}(t - (t_{\mathrm{beg},i} + \tau_i)) \big) \Big), \qquad a_{\mathbf{x},i}(\mathbf{x}) = 1 - \min \left\{ 1, \frac{\mathrm{dist}(\mathbf{x}, \overline{\Omega}_{\mathrm{stim},i})}{l_{\mathrm{exc}}} \right\}, \tag{4}$$

where $s_{\mathrm{ext}} \in \mathbb{R}$ is a constant scaling factor and where the stimulus area is extended by $\Omega_{\mathrm{stim},i} \subset \Omega_{\mathrm{exc},i} \subset \overline{\Omega}$ in all directions approximately by the length l_{exc} (see Fig. B2 in the appendix). With this choice, the external stimulus I_{ext} defined in (3) is smooth in time and both continuous and weakly differentiable in space. Alternatively, for simulations of a single heartbeat, the external stimulus can be replaced by suitable initial data v^0 of the transmembrane voltage, see, e.g., [3, 13].

The gating mechanisms at the membrane are described by the dimensionless vector $\mathbf{w} = (w_1, \dots, w_6)$. Depending on non-negative opening and closing rates $\alpha_k(v)$ and $\beta_k(v)$, the evolution is determined by

$$\mathbf{G_w}(v, \mathbf{w}) = \Big(G_k(v, w_k) \Big)_{k=1,\dots,6} \qquad \text{with} \qquad G_k(v, w_k) = \alpha_k(v) - \big(\alpha_k(v) + \beta_k(v) \big) w_k, \qquad k = 1, \dots, 6. \tag{5}$$

Starting with $w_k(0, \mathbf{x}) \in [0, 1]$, we obtain $w_k(t, \mathbf{x}) \in [0, 1]$ by construction from $G_k(v, 0) \geq 0$ and $G_k(v, 1) \leq 0$.

The evolution of the calcium concentration depends on the ionic current I_s and is of the form

$$G_c(v, c, \mathbf{w}) = -\alpha_c I_s(v, c, w_1, w_2) + w_c(\alpha_c - c). \tag{6}$$

All parameters, the explicit equations for the ionic currents, and the opening and closing rates for the Beeler–Reuter model are summarized in the App. A.

2.1 | Existence and uniqueness

Franzone and Savaré [1] studied the well-posedness for the bidomain equations coupled to the phenomenological cubic FitzHugh–Nagumo model. By exploiting the structure of this simple ODE they were able to use a variational formulation. Based on the Fedo–Galerkin method, Bendahmane and Karlsen [25] proved existence and uniqueness for the bidomain model by omitting the coupling to an ODE system representing the gating mechanisms and the evolution of intracellular ion concentrations. Also for the macroscopic bidomain equations, Bourgault, Coudière and Pierre [26] used semigroup techniques to show well-posedness for coupling with different cell models including Aliev–Panfilov [27] and McCulloch [28]. Veneroni [29] introduced an existence and uniqueness result for the bidomain model extending the class of models at the cellular level, in particular including the original Luo–Rudy model [30]. The assumptions on the cellular model, however, are not fulfilled for the Beeler–Reuter model. For example, Veneroni requires the existence of a positive continuous function depending on the gating vector $\mathbf{w}$ bounding the derivative of the slow inward current from below. Additionally, the sum of the remaining currents has to be Lipschitz continuous. Both assumptions cannot be achieved for the Beeler–Reuter model within the function spaces considered by Veneroni.

For the bidomain model coupled to the Morris–Lecar model [31], Paragaei and Kumar [32] proved the existence using a Fedo–Galerkin/compactness argument and the uniqueness based on Gronwall's Lemma.

For the monodomain model in 2d coupled to the Beeler–Reuter cell model, the following result is shown in Bendahmane et al. [13, Thm. 3.1] for the case that the stimulus is included in the initial values.

Theorem 1. Let $\Omega \subset \mathbb{R}^2$ be a Lipschitz domain. Given the initial values $(v^0, c^0, \mathbf{w}^0) \in L_\infty(\Omega) \cap H^1(\Omega) \times L_\infty(\Omega) \times L_\infty(\Omega)^6$, there is a unique weak solution

$$(v, c, \mathbf{w}) \in L_\infty\big((0, T) \times \Omega\big) \cap L_2\big(0, T; H^1(\Omega)\big) \times L_\infty\big((0, T) \times \Omega\big) \times \big(L_\infty((0, T) \times \Omega)\big)^6$$

of the monodomain problem (1) with $I_{\text{ext}} = 0$ solving the variational system

$$-\int_\Omega v^0(\mathbf{x})\varphi(0, \mathbf{x})\, d\mathbf{x} + \int_{(0,T)} \int_\Omega (-v\partial_t\varphi + \mathbf{D}\nabla v \cdot \nabla\varphi)\, d\mathbf{x}\, dt = \int_{(0,T)} \int_\Omega -I_{\text{ion}}(v, c, \mathbf{w})\varphi\, d\mathbf{x}\, dt,$$

$$-\int_\Omega w_{0,k}(\mathbf{x})\psi_k(0, \mathbf{x})\, d\mathbf{x} + \int_{(0,T)} \int_\Omega -w_k\partial_t\psi_k\, d\mathbf{x}\, dt = \int_{(0,T)} \int_\Omega G_k(v, w_k)\psi_k\, d\mathbf{x}\, dt, \qquad k = 1, \dots, 6,$$

$$-\int_\Omega c^0(\mathbf{x})\eta(0, \mathbf{x})\, d\mathbf{x} + \int_{(0,T)} \int_\Omega -c\partial_t\eta\, d\mathbf{x}\, dt = \int_{(0,T)} \int_\Omega G_c(v, c, \mathbf{w})\eta\, d\mathbf{x}\, dt$$

for smooth test functions $\varphi, \psi_k, \eta \in C^1([0, T] \times \overline{\Omega})$ with $\varphi(T) = \psi_k(T) = \eta(T) = 0$.

The proof relies on the approximation of $(v_h, c_h, \mathbf{w}_h)$ in space and time with modified control volume finite elements and implicit time integration. Additionally, a discrete maximum principle is established. Then, it is shown that a weak limit exists, and that the discrete solutions are bounded a.e. in $(0, T) \times \Omega$ by

$$v_{\min} \leq v_h \leq v_{\max}, \qquad 0 \leq c_{\min} \leq c_h \leq c_{\max}, \qquad 0 \leq w_{k,h} \leq 1, \quad k = 1, \dots, 6$$

with $v_{\min}, v_{\max}, c_{\min}, c_{\max} \in \mathbb{R}$. As the external current in (1) is only applied for a short time at the beginning, the result transfers also to our configuration for the remaining time interval and modified initial values.

Assuming more regularity and smooth data, the semigroup approach in Veneroni [29, Lem. 3.3] yields continuity of the solution.

3 | NUMERICAL APPROXIMATION OF THE MONODOMAIN EQUATION

The PDE-ODE system (1) is discretized in space by conforming finite elements for the voltage v and nodal values for $(c, \mathbf{w})$. For the time discretization we discuss and compare different splitting methods. All methods discribed in Sec. 3.2 are based on the component-wise. The difference is the way how the PDE for the transmembrane voltage is treated.

3.1 | Discretization in space

Let $\Omega_h = \bigcup_{K \in \mathcal{K}_h} K$ be a decomposition into open tetrahedra, and let $V_h = \{\phi_h \in C^0(\overline{\Omega}) : \phi_h|_K \in \mathbb{P}_1(K) \text{ for all } K \in \mathcal{K}_h\}$ be the approximation space of lowest order conforming finite elements. All functions $\phi_h \in V_h$ are uniquely defined by their nodal values $(\phi_h(\mathbf{x}))_{\mathbf{x} \in \mathcal{N}_h}$ at the corner points $\mathcal{N}_h \subset \overline{\Omega}$ of the triangulation. Let $\Pi_h : C^0(\overline{\Omega}) \to V_h$ be the corresponding nodal interpolation defined by $\Pi_h(\phi)(\mathbf{x}) = \phi(\mathbf{x})$ for $\mathbf{x} \in \mathcal{N}_h$. Let V_h' be the dual space of V_h, and let $\langle \cdot, \cdot \rangle$ denote the dual pairing.

We define $M_h, A_h \in \mathcal{L}(V_h, V_h')$ by

$$\langle M_h \phi_h, \psi_h \rangle = \int_\Omega \phi_h \psi_h \, d\mathbf{x}, \qquad \langle A_h \phi_h, \psi_h \rangle = \chi^{-1} \int_\Omega (\mathbf{D} \nabla \phi_h) \cdot \nabla \psi_h \, d\mathbf{x}, \qquad \phi_h, \psi_h \in V_h.$$

The discrete operators M_h and A_h are represented as (parallel distributed) matrices and are assembled only once. The extension of the operator M_h to $M \in \mathcal{L}(L_2(\Omega), V_h')$ defined by

$$\langle M \phi, \psi_h \rangle = \int_\Omega \phi \psi_h \, d\mathbf{x}, \qquad \phi \in L_2(\Omega), \ \psi_h \in V_h$$

can be realized only approximately. For continuous functions ϕ, $M\phi$ can be approximated by $M_h \Pi_h \phi$. Alternatively, it can be approximated by the numerical integration operator $\mathcal{M}_h \in \mathcal{L}(C^0(\overline{\Omega}), V_h')$ defined by a quadrature rule

$$\langle \mathcal{M}_h \phi, \psi_h \rangle = \sum_{K \in \mathcal{K}_h} \sum_{q=1}^{n_{\text{quad}}} \omega_{K,q} \phi(\mathbf{x}_{K,q}) \psi_h(\mathbf{x}_{K,q}), \qquad \phi \in C^0(\overline{\Omega}), \psi_h \in V_h$$

with weights $\omega_{K,q} > 0$ and integration points $\mathbf{x}_{K,q} \in K$ for $q = 1, \dots, n_{\text{quad}}$, so that $\mathcal{M}_h \phi_h = M_h \phi_h$ for $\phi_h \in V_h$. We will show in our evaluation of different schemes that using numerical quadrature $\mathcal{M}_h \phi_h$ instead of interpolation $M_h \Pi_h \phi$ improves the stability in case that ϕ is not smooth enough. In the terminology introduced by Pathmanathan et al.[15], the evaluation by the approximative L_2 integral corresponds to the state variable interpolation (SVI), and the Lagrange interpolation is the ionic current interpolation (ICI).

The semi-discrete equation in space determines $(v_h, c_h, \mathbf{w}_h) : [0, T] \to V_h^8$ by

$$C_m M_h \partial_t v_h + A_h v_h + \mathcal{M}_h I_{\text{ion}}(v_h, c_h, \mathbf{w}_h) = \mathcal{M}_h I_{\text{ext}} \qquad \text{in } V_h', \tag{7a}$$

$$\partial_t c_h - G_c(v_h, c_h, \mathbf{w}_h) = 0 \qquad \text{for all } \mathbf{x} \in \mathcal{N}_h, \tag{7b}$$

$$\partial_t \mathbf{w}_h - \mathbf{G_w}(v_h, \mathbf{w}_h) = \mathbf{0} \qquad \text{for all } \mathbf{x} \in \mathcal{N}_h \tag{7c}$$

subject to the initial values at $t = 0$

$$v_h(0, \mathbf{x}) = v^0(\mathbf{x}), \qquad c_h(0, \mathbf{x}) = c^0(\mathbf{x}), \qquad \mathbf{w}_h(0, \mathbf{x}) = \mathbf{w}^0(\mathbf{x}), \qquad \mathbf{x} \in \mathcal{N}_h \tag{7d}$$

obtained by nodal interpolation of (1d), where we assume that the initial data $(v^0, c^0, \mathbf{w}^0)$ are continuous. For the numerical experiments in Sec. 4 the initial conditions are constant in space. Note, that for the ODE evolution in (7b) and (7c) the evaluation at the nodal points $\mathcal{N}_h$ is sufficient, but in general the application of $\mathcal{M}_h$ in (7a) requires the evaluation of $(c_h, \mathbf{w}_h)$ at the integration points in every cell $K \in \mathcal{K}_h$.

3.2 | Discretization in time

Let $N \in \mathbb{N}$ be the number of time steps, let $\Delta t = T/N$ be the step-size of the time discretization, and set $t_n = n\Delta t$. Starting with $(v_h^0, c_h^0, \mathbf{w}_h^0)$ given by (7d), we now present different methods for computing the next iterate $(v_h^n, c_h^n, \mathbf{w}_h^n)$ from the approximations $(v_h^{n-1}, c_h^{n-1}, \mathbf{w}_h^{n-1})$ in the previous time step.

It is well-known that the space discretization of the PDE (1a) leads to a stiff ODE system. If an explicit Runge–Kutta or multi-step method is applied to this ODE, then an extremely small step-size has to be used in order to ensure stability. Such a severe step-size restriction can be avoided by using an A-stable or $A(\alpha)$-stable time integrator instead, but such methods are implicit. This means that in every time step a nonlinear system of equations has to be solved. Applying such a method to the *full* system (1) is thus computationally very expensive. Another numerical challenge is the fast switching of the gating variables. If the solution of (1c) is approximated, say, with a Runge–Kutta method, then again a very small step-size has to be chosen to obtain an acceptable accuracy.

For these reasons the component-wise splitting is very popular and widely used [13, 14]. In this approach every time step for propagating the system (7) consists of three sub-steps. In each of these sub-steps, only *some* of the unknowns are updated, while the others are kept fixed: first, the gating variables are updated, then the calcium concentration, and finally the transmembrane voltage. Interchanging the order of these three sub-steps is possible and yields a different but similar method with nearly the same accuracy.

1) Exact propagation of the gating variables.

For fixed transmembrane voltage v_h^{n-1} the ODE (1c) for the gating variables is linear in $\mathbf{w}$ and decoupled in all components (see (5)). In (7c) the ODE for given $(v_h^{n-1}, \mathbf{w}_h^{n-1})$ takes the form

$$\partial_t w_{h,k} = \alpha_k(v_h^{n-1}) - \big(\alpha_k(v_h^{n-1}) + \beta_k(v_h^{n-1})\big) w_{h,k} \quad \text{for} \quad t \in (t_{n-1}, t_n) \quad \text{with} \quad w_{h,k}(t_{n-1}) = w_{h,k}^{n-1}, \ k = 1, \dots, 6.$$

This can be solved exactly, so that we get $w_{h,k}(t_n) = \varphi_k^{\Delta t}(v_h^{n-1}, w_{h,k}^{n-1})$ with

$$\varphi_k^{\Delta t}(v_h, w_{h,k}) = w_{k,\infty}(v_h) + \big(w_{h,k} - w_{k,\infty}(v_h)\big) \exp\big(-\Delta t (\alpha_k(v_h) + \beta_k(v_h))\big), \qquad w_{k,\infty}(v) = \frac{\alpha_k(v_h)}{\alpha_k(v_h) + \beta_k(v_h)}. \tag{8}$$

This defines $\mathbf{w}_h^n = \boldsymbol{\varphi}^{\Delta t}(v_h^{n-1}, \mathbf{w}_h^{n-1})$ with $\boldsymbol{\varphi}^{\Delta t} = \big(\varphi_k^{\Delta t}\big)_{k=1,\dots,6}$.

2) Explicit Euler method for the calcium concentration.

The ODE (7b) for the calcium concentration is not stiff. Hence, for given $(v_h^{n-1}, c_h^{n-1}, \mathbf{w}_h^n)$, we can simply update c_h^{n-1} with one step of the explicit Euler method

$$c_h^n = c_h^{n-1} + \Delta t \, G_c(v_h^{n-1}, c_h^{n-1}, \mathbf{w}_h^n). \tag{9}$$

3) Time stepping for the transmembrane voltage.

In the third sub-step the solution of the semi-linear parabolic equation

$$C_{\mathrm{m}} M_h \partial_t v_h + A_h v_h + F(t, v_h, c_h^n, \mathbf{w}_h^n) = 0 \quad \text{for} \quad t \in (t_{n-1}, t_n) \quad \text{with} \quad v_h(t_{n-1}) = v_h^{n-1} \tag{10}$$

with $F(t, v_h, c_h, \mathbf{w}_h) = \mathcal{M}_h\big(I_{\mathrm{ion}}(v_h, c_h, \mathbf{w}_h) - I_{\mathrm{ext}}(t, \cdot)\big)$ has to be approximated for given $(v_h^{n-1}, c_h^n, \mathbf{w}_h^n)$.
We compare several options:

(GS) A standard approach for the monodomain problem is the Godunov splitting: with $\partial_t v_h \approx (\Delta t)^{-1}\big(v_h^n - v_h^{n-1}\big)$ and $F(t, v_h, c_h, \mathbf{w}_h) \approx M_h \Pi_h\big(I_{\mathrm{ion}}(v_h, c_h, \mathbf{w}_h) - I_{\mathrm{ext}}(t, \cdot)\big)$, we can introduce an intermediate update $v_h^{n-1/2}$ and define

$$v_h^{n-1/2} = v_h^{n-1} - \Delta t \, C_{\mathrm{m}}^{-1}\big(I_{\mathrm{ion}}(v_h^{n-1}, c_h^n, \mathbf{w}_h^n) - I_{\mathrm{ext}}(t_n, \cdot)\big), \tag{11a}$$

$$\big(C_{\mathrm{m}} M_h + \Delta t \, A_h\big) v_h^n = C_{\mathrm{m}} M_h v_h^{n-1/2}. \tag{11b}$$

This corresponds to one step of the Lie–Trotter splitting applied to (10). In this form it is realized, e.g., in openCARP [33]. For our tests we improve the approximation of the external current I_{ext} by numerical integration, i.e.,

$$v_h^{n-1/2} = v_h^{n-1} - \Delta t \, C_{\mathrm{m}}^{-1} I_{\mathrm{ion}}(v_h^{n-1}, c_h^n, \mathbf{w}_h^n), \tag{12a}$$

$$\big(C_{\mathrm{m}} M_h + \Delta t \, A_h\big) v_h^n = C_{\mathrm{m}} M_h v_h^{n-1/2} + \Delta t \, \mathcal{M}_h I_{\mathrm{ext}}(t_n, \cdot). \tag{12b}$$

In comparison with other splitting schemes we use (12) to exclude the error from the difference $(M_h \Pi_h - \mathcal{M}_h) I_{\mathrm{ext}}$ in the evaluation of the external current.

As an alternative to (GS) the following implicit methods are considered:

(IE-SVI) The implicit Euler method computes the approximation v_h^n by solving the nonlinear equation

$$\left(C_{\mathrm{m}} M_h + \Delta t\, A_h\right) v_h^n - C_{\mathrm{m}} M_h v_h^{n-1} + \Delta t\, F(t_n, v_h^n, c_h^n, \mathbf{w}_h^n) = 0 \tag{13}$$

with several Newton steps.

(LI-SVI) If only one single Newton step is used, then this yields the linear implicit scheme

$$\left(C_{\mathrm{m}} M_h + \Delta t\, A_h + \Delta t\, \partial_v F(t_n, v_h^{n-1}, c_h^n, \mathbf{w}_h^n)\right) v_h^n = C_{\mathrm{m}} M_h v_h^{n-1} + \Delta t\left(\partial_v F(t_n, v_h^{n-1}, c_h^n, \mathbf{w}_h^n) v_h^{n-1} - F(t_n, v_h^{n-1}, c_h^n, \mathbf{w}_h^n)\right) \tag{14}$$

with $\partial_v F(t_n, v_h, c_h, \mathbf{w}_h) = \mathcal{M}_h \partial_v I_{\mathrm{ion}}(v_h, c_h, \mathbf{w}_h)$.

(SI-SVI) If only the linear part of (10) is treated with the implicit Euler method, whereas the nonlinear part is updated with the explicit Euler method, then this leads to the semi-implicit method

$$\left(C_{\mathrm{m}} M_h + \Delta t\, A_h\right) v_h^n = C_{\mathrm{m}} M_h v_h^{n-1} - \Delta t\, F(t_n, v_h^{n-1}, c_h^n, \mathbf{w}_h^n). \tag{15}$$

The SI-SVI differs from (12) only in evaluation of total ionic current, where $M_h \Pi_h I_{\mathrm{ion}}(v_h, c_h, \mathbf{w}_h)$ is replaced by $\mathcal{M}_h I_{\mathrm{ion}}(v_h, c_h, \mathbf{w}_h)$.

The finite element matrix $C_{\mathrm{m}} M_h + \Delta t A_h$ is identical for all time steps and has to be assembled only once if the Godunov splitting (GS) or the semi-implicit method (SI-SVI) are used in the third sub-step 3). For the linear implicit scheme (LI-SVI) we have to assemble and add the derivative of F in every time step. The implicit Euler method (IE-SVI) is even more demanding, because here this has to be done in each iteration of Newton's method. For the SVI method, the right-hand side $F(t, v_h, c_h, \mathbf{w}_h) = \mathcal{M}_h\left(I_{\mathrm{ion}}(v_h, c_h, \mathbf{w}_h) - I_{\mathrm{ext}}(t, \cdot)\right)$ has to be assembled in every time step. This can be simplified by the approximation $F(t, v_h, c_h, \mathbf{w}_h) \approx M_h \Pi_h\left(I_{\mathrm{ion}}(v_h, c_h, \mathbf{w}_h) - I_{\mathrm{ext}}(t, \cdot)\right)$ using nodal interpolation (ICI) and then multiplication with the sparse mass matrix M_h; this is realized by the Godunov splitting (11).

The ODEs (7b) and (7c) are solved in parallel at all nodal points $\mathbf{x} \in \mathcal{N}_h$. The only global interaction is the solution of the PDE (7a) in every time step. In case of the Godunov splitting (12a) is solved in parallel for all nodal points and only for the diffusion part (12b) a global interaction is present.

The splitting method described above is a Lie–Trotter splitting, where the three sub-problems 1)-3) are propagated one after another with the same step-size Δt. The Lie–Trotter splitting is a first-order method, i.e., the error of the time integration is $\mathcal{O}(\Delta t)$ under certain regularity assumptions on the exact solution. A second-order method with error $\mathcal{O}(\Delta t^2)$ could, in principle, be obtained if the three sub-steps were arranged in a symmetric way, and if the numerical schemes in each of the sub-steps were replaced by second-order schemes. However, each time step of a second-order method is more costly than a step with a first-order method. Typically one expects that the higher costs per time step are compensated by a higher accuracy, such that a much larger step-size and thus a smaller number of time steps can be chosen. But this is only true if the problem is sufficiently regular, and such a degree of regularity cannot be expected for the problem (1). This is the reason why we consider only first-order time integration in this work. Since the component-wise splitting is a first-order method, it does not give much of an improvement to replace the explicit Euler method in step 2) by a higher-order Runge–Kutta method; this is confirmed by numerical tests (this can be reproduced with our code in the git repository [34] by changing the calcium update in the staggered scheme).

Splitting (and other) methods for advection-diffusion-reaction equations have been discussed in [35]. A mathematically rigorous error analysis of different splitting methods for various types of nonlinear parabolic PDEs can be found, e.g., in [36, 37, 38, 39, 40, 41, 42, 43]. A corresponding analysis for the setting considered in this work has, to the best of our knowledge, not been carried out so far.

4 | NUMERICAL EVALUATION OF TIME-STEPPING SCHEMES

In our numerical investigations, we consider, in a first step, a benchmark configuration in form of a truncated ellipsoid, where the excitation is initiated at the bottom by an external current which is smooth in space and time. The accuracy and efficiency of the different schemes are measured by the evolution of the transmembrane voltage at several test points. In a second step, we perform a convergence test in space and time, by evaluating the activation time on a realistic bi-ventricular domain. We include a physiological stimulation model representing the effect of the His-Purkinje system and use the semi-implicit scheme.

We start with a precise definition of the test configuration. Then, we provide a reference solution which is used for the evaluation of the different approaches. Finally, we test numerically the convergence in space and time of the activation time for a full bi-ventricular geometry.

4.1 | Benchmark configuration for the monodomain model

In the computational domain Ω we prescribe fiber directions $\mathbf{f} : \Omega \to \mathbb{R}^3$ which define the conductivity tensor in (1a)

$$\mathbf{D}(\mathbf{x}) = D_l \mathbf{f}(\mathbf{x}) \otimes \mathbf{f}(\mathbf{x}) + D_t\big(\mathbf{I} - \mathbf{f}(\mathbf{x}) \otimes \mathbf{f}(\mathbf{x})\big) \in \mathbb{R}^{3\times3}_{\text{sym}}, \qquad \mathbf{x} \in \overline{\Omega}, \tag{16}$$

depending on the conductivities D_l and D_t in longitudinal and transversal direction (see App. B.1). To avoid a reduction of the regularity, we use in our simulations only the space and time continuous version of I_{ext} defined in (4).

For the convergence tests, we consider the transmembrane voltage $v(t, \mathbf{z}_k)$ in $(0, T)$ at selected points $\mathbf{z}_k \in \overline{\Omega}$. Furthermore, we determine the activation time at these points $\mathbf{z}_k$, which is a frequently used quantity in the comparison of different cell models. In this benchmark scenario, we use an ellipsoid approximating the human ventricle, where the geometry is truncated and the final time $T = 30\,\text{ms}$ is chosen so that all evaluation points are activated in $(0, T)$. The evaluation points $\mathbf{z}_k$ for the truncated ellipsoid are illustrated in Fig. 1 (yellow dots) as well as the stimulus area Ω_{exc} for the discrete external current on the coarse grid. In this test, we use only one stimulation area, i.e., $n_{\text{stim}} = 1$. The position of the evaluation points $\mathbf{z}_k$ are described in detail in Tab. B2.
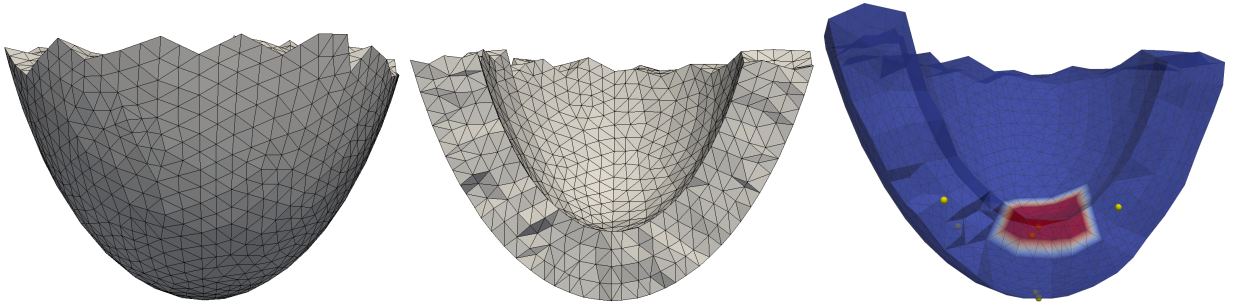

FIGURE 1 Geometry and coarse mesh on level $\ell = 0$ for the truncated ellipsoid (left and middle), activation area $\Omega_{\text{exc},1}$ and evaluation points $\mathbf{z}_k$ (right).

As a first test geometry, we used an idealized left ventricle based on the truncated ellipsoid defined in [12] with a fiber orientation ranging from $-90°$ at the epicardial surface to $+90°$ at the endocardial surface. Furthermore, the geometry was truncated closer to the apex to reduce the computational load and discretized with a tetrahedral mesh.

Let $h_0 > 0$ be the mesh size of the coarse mesh, and let Δt_0 be a time step-size which resolves the evolution on the coarse mesh. The convergence is investigated by refining in space with mesh size $h_\ell = 2^{-\ell} h_0$ on space level $\ell \in \mathbb{N}_0$ and in time with $\Delta t_j = 2^{-j} \Delta t_0$ on time level $j \in \mathbb{N}_0$, see Tab. 1. The corresponding discrete solution is denoted by $v^{j,\ell}$. The distribution of the edge length $\triangle x$ of the tetrahedral elements of the truncated ellipsoid is plotted for $\ell = 0$. For the higher levels, the distribution will be the same, only the absolute values of $\triangle x$ is halved with every refinement.

TABLE 1 Mesh data for the space levels ℓ for the truncated ellipsoid configuration and time discretization on time levels j. Here, $\triangle x$ is the length between two nodes of the mesh in mm. The figure on the right shows the relative frequency of different edge lengths in the mesh for $\ell = 0$.

ℓ	min $\triangle x$	max $\triangle x$	# cells	# vertices	j	N_j	$\triangle t_j$ (ms)
0	0.22682	1.26099	18 136	3 954	0	300	0.1
1	0.11341	0.63049	145 088	27 851	1	600	0.05
2	0.05670	0.31524	1 160 704	208 021	2	1 200	0.025
3	0.02835	0.15762	9 285 632	1 605 673	3	2 400	0.0125
4	0.01417	0.07881	74 285 056	12 612 689	4	4 800	0.00625
5	0.00708	0.03940	594 280 448	99 973 281	5	9 600	0.003125
6	0.00354	0.01970	4 754 243 584	796 078 401	6	19 200	0.0015625
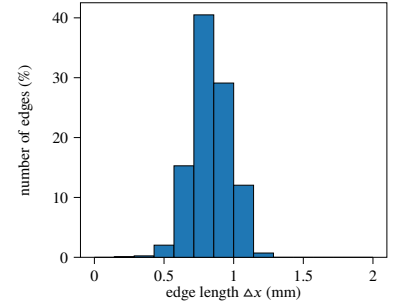
All numerical experiments are performed on the high performance computing system HoreKa at KIT using the partition *cpuonly*. The problem is solved with the open source parallel finite element system M++ [34]. The number of parallel processes was between 64 and 8192 depending on the problem size and memory requirements. The scalability of the results regarding the CPU time is ensured, see, e.g., Tab. 2 for a test with fixed levels in space and time respectively.

TABLE 2 CPU time for different number of processes for the semi-implicit (SI-SVI) approach, fixed space level $\ell = 3$ and fixed time level $j = 3$ with the benchmark configuration.

procs	64	128	256	512	1024
CPU time (hours:minutes:seconds)	1:10:49	31:54	15:54	8:33	5:11

4.2 | The reference solution

On the ellipsoidal benchmark configuration with mesh sizes and time step-sizes as defined in Tab. 1, the errors in space and time for the linear-implicit scheme (LI-SVI) are balanced even for coarse space discretizations, and we can observe the expected convergence orders in space and time. Nevertheless, the semi-implicit scheme (SI-SVI) is more accurate for the same discretizations, even if the space error is dominant and the time convergence cannot be observed for larger step-sizes. The observations for the LI-SVI and the SI-SVI are now investigated in detail by comparing the approximations of the transmembrane voltage computed with very fine discretizations in space and time for both time integration methods. By extrapolation in space and time, we estimate the accuracy of the evolution of the transmembrane voltage at selected points.

In Fig. 2, the evolution of the transmembrane voltage at $\mathbf{z}_4, \mathbf{z}_5, \mathbf{z}_6, \mathbf{z}_7 \in \Omega$ and the convergence in space and in time at $\mathbf{z}_6$ is shown for LI-SVI. The excitation wave arrives in the expected sequence depending on the fiber directions and the distances to the stimulus located in Ω_{stim}.
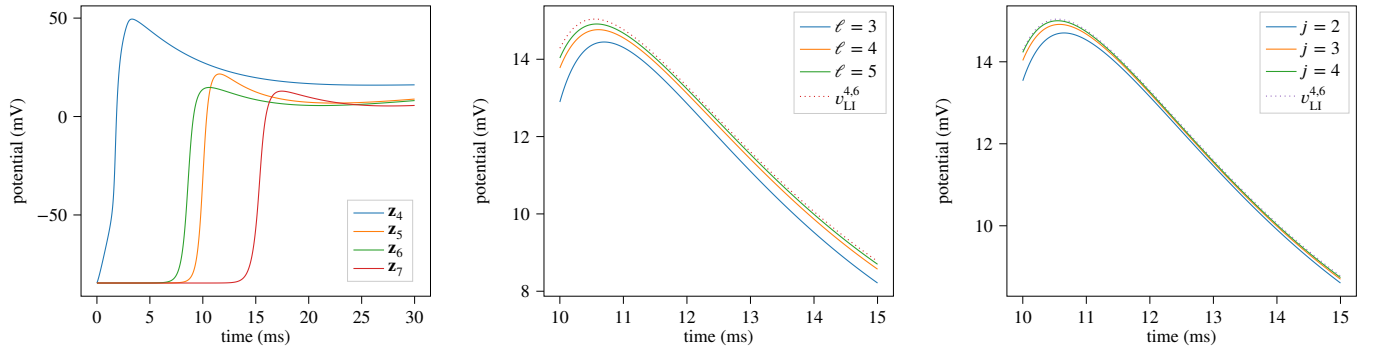

FIGURE 2 Evolution of the transmembrane voltage v at the different evaluation points $\mathbf{z}_k \in \Omega$ of the benchmark configuration (cf. Fig. 1) computed with the LI-SVI, and convergence of the LI-SVI scheme to the reference solution in space with fixed $j = 3$ and in time with fixed $\ell = 5$ evaluated for $v_{\text{LI}}^{j,\ell}(t, \mathbf{z}_6)$, $t \in [10, 15]$ ms.

The computation of the error for the finest approximations of LI-SVI and SI-SVI is based on the estimate of the convergence order in space and time. From the differences of the solutions in space $v^{j,\ell}(\cdot, \mathbf{z}_k) - v^{j,\ell-1}(\cdot, \mathbf{z}_k)$ and in time $v^{j,\ell}(\cdot, \mathbf{z}_k) - v^{j-1,\ell}(\cdot, \mathbf{z}_k)$, cf. Tab. 3, the asymptotic convergence rate can be estimated from the factors $f_{j,\ell}$ and $g_{j,\ell}$ defined by

$$f_{j,\ell} = \frac{\|v^{j,\ell-1} - v^{j,\ell-2}\|_{L_2(0,T)}}{\|v^{j,\ell} - v^{j,\ell-1}\|_{L_2(0,T)}} \approx 2^{\text{order space}}, \quad g_{j,\ell} = \frac{\|v^{j-1,\ell} - v^{j-2,\ell}\|_{L_2(0,T)}}{\|v^{j,\ell} - v^{j-1,\ell}\|_{L_2(0,T)}} \approx 2^{\text{order time}}.$$

Using extrapolation (see, e.g., [44, Chap. 4.2.8]), the limit approximations in space $v^{j,\infty}$ and time $v^{\infty,\ell}$ for $j = 0, \dots, J$ and $\ell = 0, \dots, L$ are computed from the finest computation on $\ell = L$ and $j = J$ by

$$v^{j,\infty} = \frac{f_{j,L}}{f_{j,L} - 1} v^{j,L} - \frac{1}{f_{j,L} - 1} v^{j,L-1}, \qquad v^{\infty,\ell} = \frac{g_{J,\ell}}{g_{J,\ell} - 1} v^{J,\ell} - \frac{1}{g_{J,\ell} - 1} v^{J-1,\ell}. \tag{17}$$

For both schemes, we observe quadratic convergence in space, cf. Tab. 3. For LI-SVI, we observe linear convergence in time. This is not as good for the SI-SVI scheme, where nearly linear convergence in time is observed only for sufficiently small time steps.

TABLE 3 Convergence of $v^{j,\ell}$ in $\|\cdot\|_{L_2(0,T)}$ at $\mathbf{z}_6$ and $\mathbf{z}_7$ for the linear implicit (LI-SVI) and the semi-implicit (SI-SVI) scheme.

$j = 4$	$\ell = 4$	$\ell = 5$	$\ell = 6$	$\ell = 5$	$j = 3$	$j = 4$	$j = 5$	$j = 6$
$v_{\text{LI}}^{j,\ell}(\cdot, \mathbf{z}_6) - v_{\text{LI}}^{j,\ell-1}(\cdot, \mathbf{z}_6)$	0.1725	0.0523	0.0103	$v_{\text{LI}}^{j,\ell}(\cdot, \mathbf{z}_6) - v_{\text{LI}}^{j-1,\ell}(\cdot, \mathbf{z}_6)$	0.1507	0.0658	0.0304	-
$v_{\text{LI}}^{j,\ell}(\cdot, \mathbf{z}_7) - v_{\text{LI}}^{j,\ell-1}(\cdot, \mathbf{z}_7)$	0.5942	0.2099	0.0564	$v_{\text{LI}}^{j,\ell}(\cdot, \mathbf{z}_7) - v_{\text{LI}}^{j-1,\ell}(\cdot, \mathbf{z}_7)$	0.2785	0.1231	0.0573	-
$v_{\text{SI}}^{j,\ell}(\cdot, \mathbf{z}_6) - v_{\text{SI}}^{j,\ell-1}(\cdot, \mathbf{z}_6)$	0.1765	0.0538	0.0106	$v_{\text{SI}}^{j,\ell}(\cdot, \mathbf{z}_6) - v_{\text{SI}}^{j-1,\ell}(\cdot, \mathbf{z}_6)$	0.0174	0.0126	0.0084	0.0048
$v_{\text{SI}}^{j,\ell}(\cdot, \mathbf{z}_7) - v_{\text{SI}}^{j,\ell-1}(\cdot, \mathbf{z}_7)$	0.6049	0.2144	0.0577	$v_{\text{SI}}^{j,\ell}(\cdot, \mathbf{z}_7) - v_{\text{SI}}^{j-1,\ell}(\cdot, \mathbf{z}_7)$	0.0329	0.0092	0.0077	0.0048

Quadratic convergence in space and linear convergence in time is now used to estimate the accuracy of the finest solutions, which will be used as a reference for comparison with other schemes. This is tested for $v_{\mathrm{LI}}^{\mathrm{ref}} = v_{\mathrm{LI}}^{4,6}$ and $v_{\mathrm{SI}}^{\mathrm{ref}} = v_{\mathrm{SI}}^{5,6}$ in Tab. 4. In both cases, the extrapolates are given by

$$v^{5,\infty} = \frac{4}{3}v^{5,5} - \frac{1}{3}v^{5,4}, \qquad v^{\infty,5} = 2v^{5,5} - v^{4,5}, \qquad v^{\infty,\infty} = 2v^{5,\infty} - v^{4,\infty}.$$

TABLE 4 Estimates for the relative error for the reference solutions.

	$\dfrac{\|v^{5,\infty}(\cdot, \mathbf{z}_k) - v^{\mathrm{ref}}(\cdot, \mathbf{z}_k)\|_{L_2(0,T)}}{\|v^{5,\infty}(\cdot, \mathbf{z}_k)\|_{L_2(0,T)}}$	$\dfrac{\|v^{\infty,5}(\cdot, \mathbf{z}_k) - v^{\mathrm{ref}}(\cdot, \mathbf{z}_k)\|_{L_2(0,T)}}{\|v^{\infty,5}(\cdot, \mathbf{z}_k)\|_{L_2(0,T)}}$	$\dfrac{\|v^{\infty,\infty}(\cdot, \mathbf{z}_k) - v^{\mathrm{ref}}(\cdot, \mathbf{z}_k)\|_{L_2(0,T)}}{\|v^{\infty,\infty}(\cdot, \mathbf{z}_k)\|_{L_2(0,T)}}$
$v_{\mathrm{LI}}^{\mathrm{ref}}(\cdot, \mathbf{z}_6)$	0.0055	0.0068	0.0089
$v_{\mathrm{LI}}^{\mathrm{ref}}(\cdot, \mathbf{z}_7)$	0.0114	0.0050	0.0164
$v_{\mathrm{SI}}^{\mathrm{ref}}(\cdot, \mathbf{z}_6)$	0.0018	0.0026	0.0013
$v_{\mathrm{SI}}^{\mathrm{ref}}(\cdot, \mathbf{z}_7)$	0.0059	0.0070	0.0046

We observe that the relative error estimated by extrapolation in space (left) and in time (middle) is nearly equilibrated, and extrapolating in space and time (right) shows that the relative error of $v_{\mathrm{SI}}^{\mathrm{ref}}$ is below 0.5% in both tests points. Since $v_{\mathrm{LI}}^{\mathrm{ref}}$ is computed with larger time steps, the estimated error is larger. However, the difference of the two solutions

$$\frac{\|v_{\mathrm{LI}}^{\mathrm{ref}}(\cdot, \mathbf{z}_6) - v_{\mathrm{SI}}^{\mathrm{ref}}(\cdot, \mathbf{z}_6)\|_{L_2(0,T)}}{\|v_{\mathrm{LI}}^{\infty,\infty}(\cdot, \mathbf{z}_6)\|_{L_2(0,T)}} = 0.0089494$$

is below 1%, so that for both reference solutions the estimated error is of the same magnitude.

4.3 │ Comparison of different approximation schemes for the total ionic current

In general, we use the L_2-projection (SVI) for the evaluation of $(c_h^n, \mathbf{w}_h^n)$ in (7a). Since the ODEs in (7b) and (7c) are solved on the nodal points only, simply using Lagrange interpolation (ICI) in (7a) is numerically cheaper, but also less accurate as reported by Pathmanathan et al. [15] for the semi-implicit case (SI). Here, this is confirmed for the linear implicit scheme on the ellipsoidal benchmark configuration, cf. Tab. 5: the Lagrange interpolation takes $\approx 25\%$ less CPU time than the SVI approach. However, to achieve the same accuracy, one more space refinement is needed, which results in an approximately 12 times longer CPU time compared to the SVI on the lower level. We observe for ICI in one case ($\ell = 4$ and $j = 4$) a smaller error for this benchmark quantity than for $j \neq 4$, but the limit for smaller time steps ($j > 4$) is larger. This singular effect was also observed in [15] for different space discretizations. In summary, we conclude that the SVI approach is more efficient than ICI.

TABLE 5 Accuracy of the transmembrane potential at $\mathbf{z}_6$ for the L_2-projection (SVI) and the Lagrange interpolation (ICI) compared to $v_{\mathrm{LI}}^{\mathrm{ref}}$ (left) and the required parallel CPU time (given in hours:minutes:seconds) (right) to solve the full system of the benchmark configuration with the linear implicit scheme (LI).

$\|v^{j,\ell}(\cdot, \mathbf{z}_6) - v_{\mathrm{LI}}^{\mathrm{ref}}(\cdot, \mathbf{z}_6)\|_{L_2(0,T)}$		SVI	ICI
$\ell = 3$	$j = 3$	0.2794	0.4142
	$j = 4$	0.2330	0.6917
	$j = 5$	0.2134	0.8328
$\ell = 4$	$j = 3$	0.1140	0.2211
	$j = 4$	0.0622	0.1053
	$j = 5$	0.0485	0.2526

		SVI		ICI	
discretization		procs	CPU time	procs	CPU time
$\ell = 3$	$j = 3$	512	11:43	512	10:11
	$j = 4$	512	22:02	512	16:13
	$j = 5$	512	42:07	512	30:36
$\ell = 4$	$j = 3$	1024	1:06:44	1024	56:10
	$j = 4$	1024	2:06:18	1024	1:34:51
	$j = 5$	1024	3:39:28	1024	2:50:35

4.4 | Convergence of the conduction velocity

The space convergence behavior of the conduction velocity (CV) is investigated for the benchmark setup using the semi-implicit scheme (SI-SVI). The CV between two points $\mathbf{x}, \mathbf{y} \in \overline{\Omega}_{\text{act}}$ is defined by

$$c_{\text{vel}}(v, \mathbf{x}, \mathbf{y}) = \frac{\|\mathbf{x} - \mathbf{y}\|}{|t_{\text{act}}(v, \mathbf{x}) - t_{\text{act}}(v, \mathbf{y})|} \qquad \text{with } \overline{\Omega}_{\text{act}}(v) = \left\{ \mathbf{x} \in \Omega : v(t, \mathbf{z}) \geq v_{\text{act}} \text{ for some } t \in [0, T] \right\} \subset \overline{\Omega} \qquad (18)$$

depending on the activation time t_{act}

$$t_{\text{act}}(v, \mathbf{z}) = \min \left\{ t \in [0, T] : v(t, \mathbf{z}) \geq v_{\text{act}} \right\}, \qquad \mathbf{z} \in \overline{\Omega}_{\text{act}} \qquad (19)$$

indicating for a point $\mathbf{z}$ the time $t \in [0, T]$ when the transmembrane voltage v is larger than $v_{\text{act}} > v_0$ for the first time. We use $v_{\text{act}} = -40\,\text{mV}$ (see [10, 7]) and a spatially constant initial voltage $v_0(\mathbf{x}) = v_0 = -84.57\,\text{mV}$.
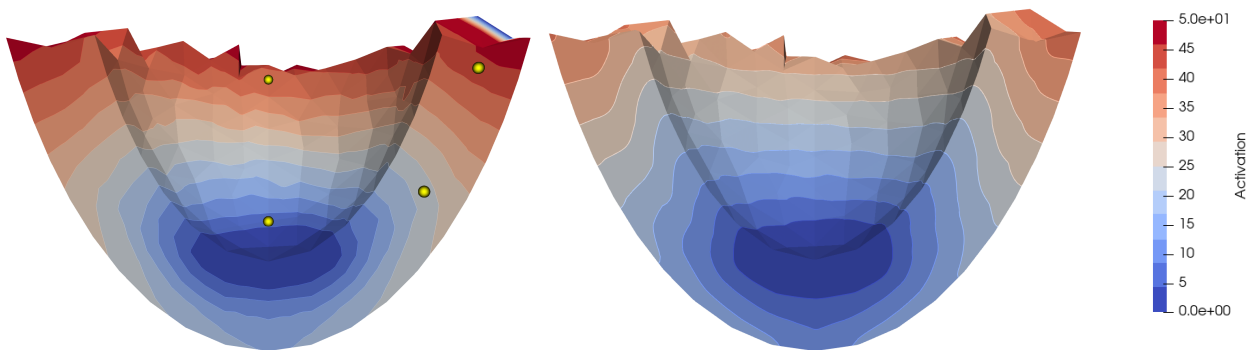

FIGURE 3 Activation pattern for $\ell = 0$ (left, including the evaluation points, cf. Tab.B2) and for $\ell = 3$ (right, both computed with fixed time level $j = 4$).

Fig. 3 shows the activation patterns in the truncated ellipsoid for two different mesh resolutions. To measure the distance between the two points in the definition of (18), we use the geodesic distance in the truncated ellipsoid. To investigate the space convergence of the CV, we choose two pairs of points $\mathbf{x}, \mathbf{y} \in \overline{\Omega}$: one pair in the center of the myocardial wall and one on the inner surface (details in Tab. B2). Fixing the step-size at $j = 4$, the conduction velocity converges linearly in space in the center of the myocardial wall and nearly linear at the inner surface points, cf. Tab. 6.

TABLE 6 Conduction velocities in m/s computed with the semi-implicit (SI-SVI) scheme on the truncated ellipsoidal mesh (left) and the convergence of the conduction velocities in space (right) both for fixed time $j = 4$.
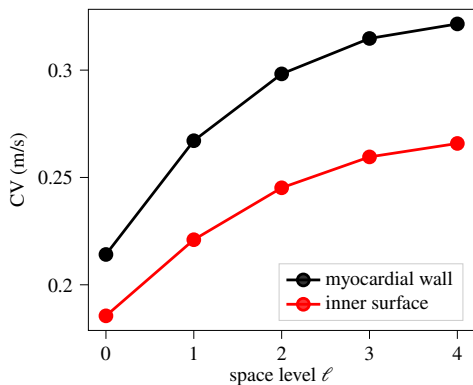
$c_{\text{vel}}(v^{j,\ell}, \mathbf{x}_k, \mathbf{y}_k) - c_{\text{vel}}(v^{j,\ell-1}, \mathbf{x}_k, \mathbf{y}_k)$	$\ell = 1$	$\ell = 2$	$\ell = 3$	$\ell = 4$
myocardial wall ($k = 1$)	0.0530	0.0311	0.0165	0.0068
inner surface ($k = 2$)	0.0355	0.0242	0.0144	0.0063

We observe, that the CV does not change significantly for space discretizations larger than $\ell = 2$. Again, the activation pattern confirms the convergence of the scheme and shows smaller activation times t_{act} for the finer space discretizations.

4.5 | Comparison of the time integration approaches for the transmembrane voltage

Next, we compare the performance of the different splitting approaches defined in Sec. 3.2. Recall that the gating variables and the calcium concentrations are approximated in exactly the same way in all methods, whereas different approaches are used for the approximation of the transmembrane voltage: the Godunov splitting GS scheme, which is used in most applications, and the three implicit schemes IE-SVI, LI-SVI, and SI-SVI. For the evaluation, we compare the parallel computing time to solve the benchmark problem and the estimated error

$$\eta_{\mathrm{SI}}(\mathbf{z}_k) = \frac{\|v^{j,\ell}(\cdot, \mathbf{z}_k) - v_{\mathrm{SI}}^{\mathrm{ref}}(\cdot, \mathbf{z}_k)\|_{\mathrm{L}_2(0,T)}}{\|v_{\mathrm{SI}}^{\mathrm{ref}}(\cdot, \mathbf{z}_k)\|_{\mathrm{L}_2(0,T)}} \tag{20}$$

with respect to the reference solution $v_{\mathrm{SI}}^{\mathrm{ref}}$. Fig. 4 shows the relation between $\eta_{\mathrm{SI}}(\mathbf{z}_6)$ and CPU time. The number of parallel processes differs for the experiments; thus, to compare the CPU times in Fig. 4, they are scaled to 256 processes by multiplying the CPU time with $\#used\,procs/256$.
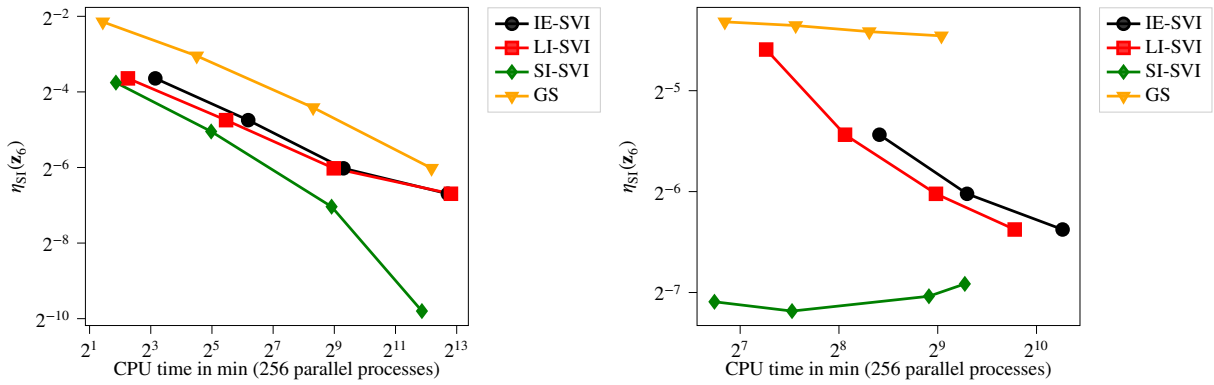

FIGURE 4 Work-precision diagram comparing the different time stepping schemes with fixed time step size with $j = 4$ for mesh levels $\ell \in \{2, 3, 4, 5\}$ (left) and with fixed mesh $\ell = 4$ for $j \in \{2, 3, 4, 5\}$ (right), where the work load is the required CPU time to solve the benchmark problem, and where the presision is estimated by $\eta_{\mathrm{SI}}(\mathbf{z}_6)$.

For a fixed step-size with $j = 4$ (cf. left panel of Fig. 4), we observe that SI-SVI is the most efficient scheme, followed by LI-SVI. The accuracy of the implicit Euler method IE-SVI and the linear implicit scheme LI-SVI are identical, because in our numerical tests it turned out that for the implicit Euler method one single Newton step was sufficient to fulfill the stopping criterion. In this case, IE-SVI and LI-SVI yield exactly the same approximation. The reason why the run-time of IE-SVI is slightly longer is that for the LI-SVI scheme a more efficient assembling routine is realized: the semi-implicit part $B_h^{\Delta t} = C_{\mathrm{m}} M_h + \Delta t A_h$ of the linearization is assembled only once, and in every time step only the nonlinear part of the linearization $\Delta t\, \partial_v F(t_n, v_h^{n-1}, c_h^n, \mathbf{w}_h^n)$ is computed in addition. This is considerably faster than assembling the full linearization in every Newton step.

For the fixed mesh level $\ell = 4$ (cf. right panel of Fig. 4), we also observe that SI-SVI is the most efficient scheme. For this test point $\mathbf{z}_6$, the error with respect to the reference solution $\eta_{\mathrm{SI}}(\mathbf{z}_6)$ is not improving for finer time steps with $j > 2$, which indicates that the error of the space discretization dominates. The computing time of the Godunov splitting GS scheme is nearly the same as for the SI-SVI scheme, but the accuracy is considerably worse. The numerical realization of the additional splitting (12b) in GS is simpler than the assembling of the right-hand side SI-SVI. On the other hand, the error is larger, e.g., the error of $v_{\mathrm{SI\text{-}SVI}}^{4,4}$ is smaller than the error of $v_{\mathrm{GS}}^{4,5}$ on the next finer mesh level. The main difference of the schemes is the approximation of the total ionic current as explained in Sec. 3.2. In summary, for our benchmark scenario the semi-implicit method SI-SVI is the most efficient scheme.

4.6 | Accuracy of the activation time on a bi-ventricular domain

For the truncated ellipsoid, we observe that SI-SVI is the most efficient scheme. Now we show that this transfers to a full bi-ventricular configuration, cf. Fig. 5. The convergence is tested by the convergence of the activation times $t_{\text{act}}(v, \mathbf{x})$ at all nodal points $\mathbf{x} \in \mathcal{N}_{h_0}$. This is evaluated for a physiological stimulation scenario at the Purkinje muscle junctions in the ventricles.
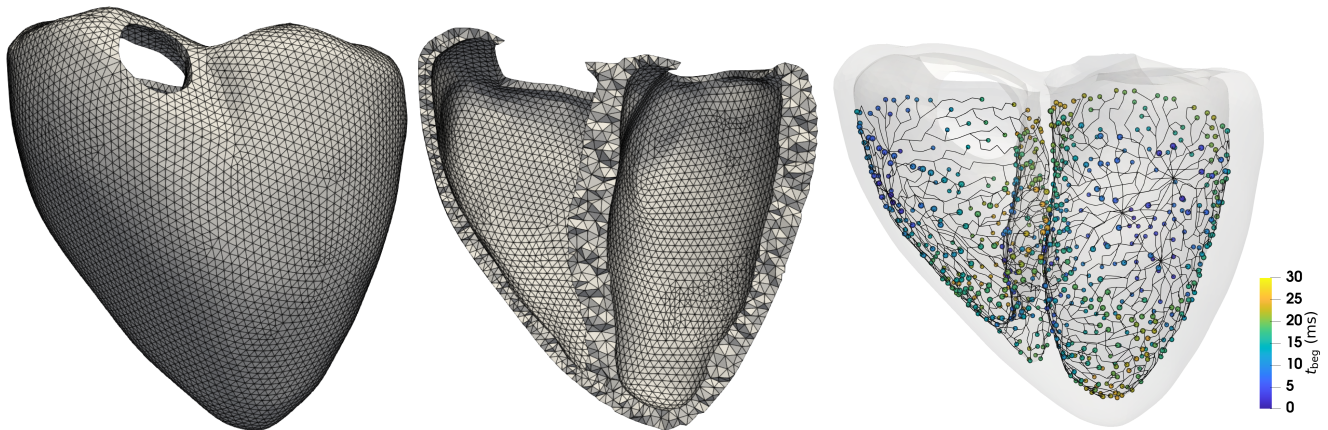

FIGURE 5 Geometry and coarse mesh on level $\ell = 0$ for the ventricles (left and middle), activation areas $\Omega_{\text{stim},i}$ and starting times $t_{\text{beg},i}$, $i = 1, \ldots, 669$ modeling the His-Purkinje system (right).

The computational domain Ω includes both ventricles. The fiber orientation is defined by a rule-based method [45, 46] with angles ranging from $-41°$ at the epicardium to $+66°$ at the endocardium in agreement with human data from diffusion tensor magnetic resonance imaging [47]. The complex stimulation of the ventricles via the His-Purkinje system is represented by the Purkinje muscle junction model [48]. Every stimulation area $\Omega_{\text{stim},i}$, $i = 1, \ldots, 669$, models a leaf of the Purkinje tree, i.e., a Purkinje muscle junction, defining $t_{\text{beg},i} \in [0.0, 0.027]$ in seconds while the amplitude $a = 30\,\text{mV}$ and the duration $\tau = 0.003\,\text{s}$ are fixed for all i. For the following numerical experiments, we use the smooth version of the external current I_{ext} in space and time as described in Sec. 4.1. We set $T = 0.16\,\text{s}$, so that in our model the full domain is activated, i.e., $\overline{\Omega} = \Omega_{\text{act}}$. The discretization data in space are given in Tab. 7, and in time we use $\Delta t_j = 2^{-j} \Delta t_0$ with $\Delta t_0 = 0.4\,\text{ms}$. The distribution of the edge length Δx is displayed for the bi-ventricular mesh at $\ell = 0$.

TABLE 7 Mesh data for the space levels ℓ for the bi-ventricular domain and time discretization on time levels j. Here Δx is the length between two nodes of the mesh, the length scale is mm. The edge length and relative frequency for the truncated ellipsoidal mesh is shown for $\ell = 0$.

ℓ	min Δx	max Δx	# cells	# vertices
0	0.365865	6.189215	102 625	24 184
1	0.182933	3.216390	821 000	164 642
2	0.091466	1.608195	6 568 000	1 204 877
3	0.045733	0.804098	52 544 000	9 196 123
4	0.022867	0.402049	420 352 000	71 809 719

j	N_j	Δt_j (ms)
0	400	0.400
1	800	0.200
2	1 600	0.100
3	3 200	0.050
4	6 400	0.025
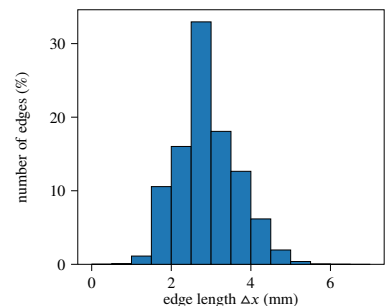
The transmembrane voltage on time level j and space level ℓ is denoted by $v^{j,\ell}$. For fixed $j = 4$, the distribution of the activation time $t_{\text{act}}(\mathbf{x}, v^{j,\ell})$, $\mathbf{x} \in \overline{\Omega}$, is displayed in Fig. 6 for $\ell = 0$ and $\ell = 2$. We observe that the depolarization wave propagates faster on the finer discretization so that the points $\mathbf{x} \in \overline{\Omega} \setminus \Omega_{\text{exc}}$ are earlier activated. As expected, $\ell = 0$ is not fine enough to reproduce the activation time (and thus also the conduction velocity) sufficiently accurate, and for $\ell = 0$ and $j = 0$ the domain is not fully activated (n.f.a.) in $(0, T)$
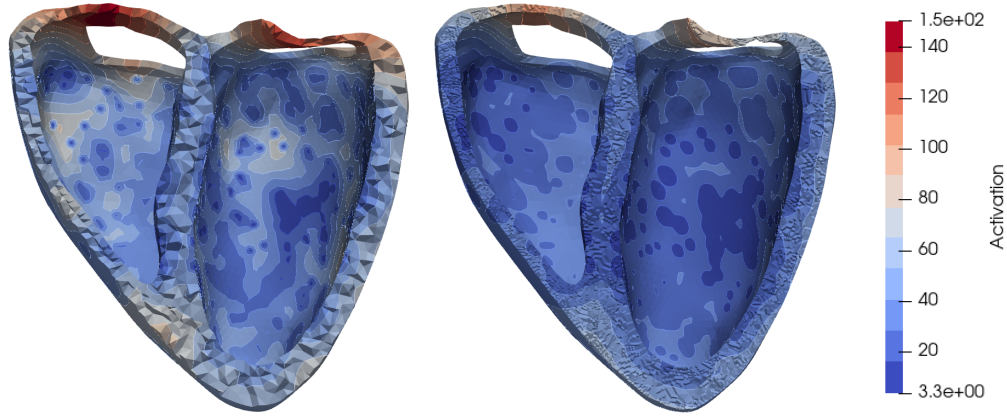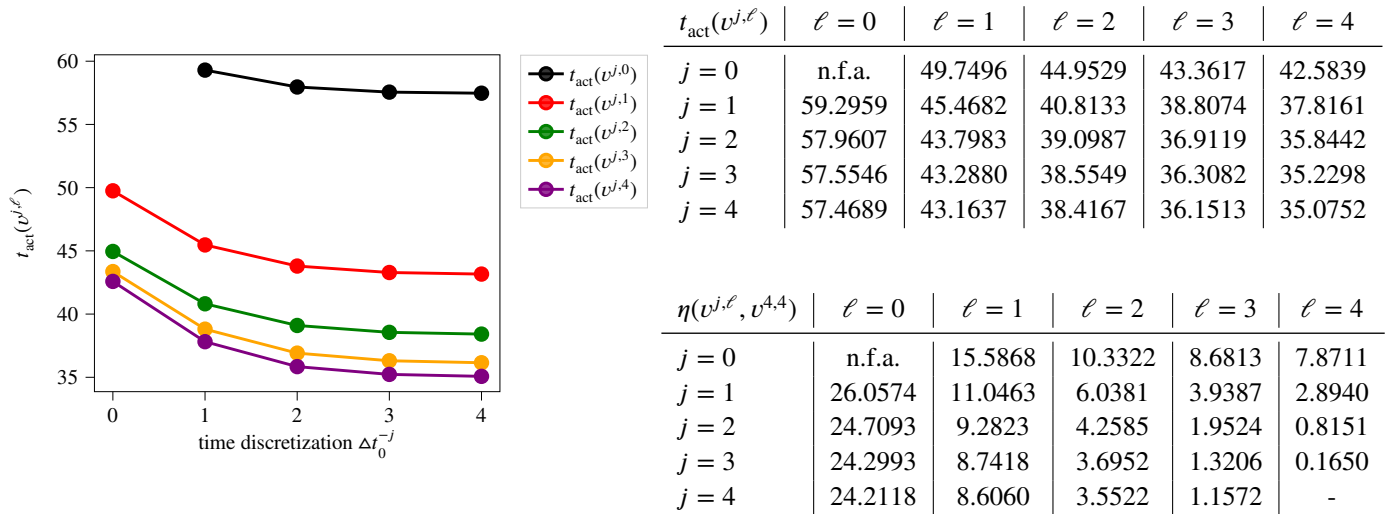
FIGURE 6 Activation pattern for the ventricles with fixed $j = 4$ with $\Delta t_j = 0.00625$ ms for $\ell = 0$ (left) and $\ell = 2$ (right).

To investigate the accuracy and convergence of the activation pattern, we compute

$$t_{\text{act}}(v) = \sqrt{\frac{1}{|\mathcal{N}_{h_0}|} \sum_{\mathbf{x} \in \mathcal{N}_{h_0}} t_{\text{act}}(v, \mathbf{x})^2}, \qquad \eta(v, w) = \sqrt{\frac{1}{|\mathcal{N}_{h_0}|} \sum_{\mathbf{x} \in \mathcal{N}_{h_0}} \left(t_{\text{act}}(v, \mathbf{x}) - t_{\text{act}}(w, \mathbf{x}) \right)^2} \qquad (21)$$

for different discretizations, cf. Tab. 8. We observe in the limit at least linear convergence in space, and the results show clearly that the error in space is dominant, so that in time the resolution for $j = 2$ is sufficient. With larger time steps the activation pattern prescribed by I_{ext} cannot be resolved, so that a minimal resolution of $\Delta t_0 = 0.4$ ms is required. By extrapolation, we can estimate that for the reference solution $v^{4,4}$ the error of $t_{\text{act}}(v^{4,4})$ is below 1%.

TABLE 8 The activation time $t_{\text{act}}(v)$ and the difference with respect to the reference solution on different levels in space and time for the semi-implicit (SI-SVI) scheme (the numbers are displayed in ms).

$t_{\text{act}}(v^{j,\ell})$	$\ell = 0$	$\ell = 1$	$\ell = 2$	$\ell = 3$	$\ell = 4$
$j = 0$	n.f.a.	49.7496	44.9529	43.3617	42.5839
$j = 1$	59.2959	45.4682	40.8133	38.8074	37.8161
$j = 2$	57.9607	43.7983	39.0987	36.9119	35.8442
$j = 3$	57.5546	43.2880	38.5549	36.3082	35.2298
$j = 4$	57.4689	43.1637	38.4167	36.1513	35.0752

$\eta(v^{j,\ell}, v^{4,4})$	$\ell = 0$	$\ell = 1$	$\ell = 2$	$\ell = 3$	$\ell = 4$
$j = 0$	n.f.a.	15.5868	10.3322	8.6813	7.8711
$j = 1$	26.0574	11.0463	6.0381	3.9387	2.8940
$j = 2$	24.7093	9.2823	4.2585	1.9524	0.8151
$j = 3$	24.2993	8.7418	3.6952	1.3206	0.1650
$j = 4$	24.2118	8.6060	3.5522	1.1572	-

The reference solution $v^{4,4}$ is computed on 4096 processor kernels in 5:18 hours.

5 | CONCLUSION

In this study, we defined a benchmark configuration on a truncated ellipsoid approximating the left ventricle. This extends the convergence tests for the conduction velocity in Woodworth et al. [10] for a rectangular domain to unstructured 3D meshes. Moreover, it also extends the results of Pathmanathan et al. [15] to the truncated ellipsoid with the linear implicit scheme instead of the semi-implicit scheme and shows that the SVI approach is more efficient than the Lagrange interpolation of the total ionic current (ICI). Additionally, we compared the convergence behavior, the accuracy and the efficiency of different time splitting schemes evaluating the transmembrane voltage.

The depolarization changes the transmembrane voltage from approximately $-90\,\mathrm{mV}$ to $20\,\mathrm{mV}$ within milliseconds, so that time step-sizes $\Delta t < 0.1$ ms are required to recover the fast dynamics. Thus, the time step is so small within the implicit Euler scheme (IE-SVI) that one Newton step is sufficient to achieve convergence, i.e., the linear implicit method (LI-SVI) and IE-SVI compute the same approximations. Additionally, we observed that an explicit evaluation of the total ionic current in the semi-implicit scheme (SI-SVI) does neither deteriorate the accuracy nor causes stability problems although the convergence region is shifted to smaller step-sizes.

The main difference of the Godunov splitting (GS) and the semi-implicit scheme is the approximation of the total ionic current I_{ion} in space, so that the better performance of SI is mainly due to the better approximation of I_{ion}.

Finally, we showed that our results for the benchmark configuration of the truncated ellipsoid transfer to a realistic setup for a bi-ventricular configuration with a complex stimulation model by a convergence study for the activation time. The activation pattern converges at least linear in space using the SI-SVI and the dominance of the space error on the coarse meshes is confirmed.

The proposed time integration schemes can be adapted by established cardiac electrophysiology simulation packages [33] and can be incorporated to a full heart electro-mechanical simulation [49].

We showed that using the semi-implicit (SI-SVI) or the linear implicit (LI-SVI) scheme will increase stability and accuracy on irregular complex coarse meshes.

Our study considers the Beeler–Reuter cell model, which covers the main physiological properties and numerical challenges. The advantages of SI-SVI or LI-SVI will transfer to more complex cell models, as the model by ten Tusscher and Panfilov [50], O'Hara and Rudy [51] or Courtemanche [52]. Since our finite element system M++ also includes nonconforming and DG approximations, future studies will investigate the synergy between modern discretization in space and optimal time stepping.

ACKNOWLEGEMENTS

References

[1] Franzone PC, Savaré G. Degenerate evolution systems modeling the cardiac electric field at micro- and macroscopic level. In: Lorenz A, Ruf B., eds. *Evolution Equations, Semigroups and Functional Analysis. Progress in Nonlinear Differential Equations and Their Applications.* Birkhäuser. 2002 (pp. 49–78)

[2] Bourgault Y, Pierre C. Comparing the bidomain and monodomain models in electro-cardiology through convergence analysis. *https://hal.archives-ouvertes.fr/hal-00545888v2* 2010.

[3] Sundnes J, Lines GT, Tveito A. An operator splitting method for solving the bidomain equations coupled to a volume conductor model for the torso. *Mathematical Biosciences* 2005; 194(2): 233–248.

[4] Qu Z, Garfinkel A. An advanced algorithm for solving partial differential equation in cardiac conduction. *IEEE Transactions on Biomedical Engineering* 1999; 46(9): 1166–1168.

[5] Rush S, Larsen H. A practical algorithm for solving dynamic membrane equations. *IEEE Transactions on Biomedical Engineering* 1978(4): 389–392.

[6] Pezzuto S, Hake J, Sundnes J. Space-discretization error analysis and stabilization schemes for conduction velocity in cardiac electrophysiology. *International Journal for Numerical Methods in Biomedical Engineering* 2016; 32(10): e02762.

[7] Woodworth LA, Cansız B, Kaliske M. Balancing conduction velocity error in cardiac electrophysiology using a modified quadrature approach. *International Journal for Numerical Methods in Biomedical Engineering* 2022: e3589.

[8] Niederer SA, Kerfoot E, Benson AP, et al. Verification of cardiac tissue electrophysiology simulators using an N-version benchmark. *Philosophical Transactions of the Royal Society A: Mathematical, Physical and Engineering Sciences* 2011; 369(1954): 4331–4351.

[9] Roy T, Bourgault Y, Pierre C. Analysis of time-stepping methods for the monodomain model. *Computational and Applied Mathematics* 2020; 39(3): 1–32.

[10] Woodworth LA, Cansız B, Kaliske M. A numerical study on the effects of spatial and temporal discretization in cardiac electrophysiology. *International Journal for Numerical Methods in Biomedical Engineering* 2021; 37(5): e3443. doi: 10.1002/cnm.3443

[11] Krishnamoorthi S, Sarkar M, Klug WS. Numerical quadrature and operator splitting in finite element methods for cardiac electrophysiology. *International Journal for Numerical Methods in Biomedical Engineering* 2013; 29(11): 1243–1266.

[12] Land S, Gurev V, Arens S, et al. Verification of cardiac mechanics software: benchmark problems and solutions for testing active and passive material behaviour. *Proc. R. Soc. Lond. A* 2015; 471(2184). doi: 10.1098/rspa.2015.0641

[13] Bendahmane M, Mroue F, Saad M. A positive cell vertex Godunov scheme for a Beeler–Reuter based model of cardiac electrical activity. *Numerical Methods for Partial Differential Equations* 2021; 37(1): 262–301.

[14] Caligari S, Scacchi S. Mathematical and numerical modeling of reentrant ventricular arrhythmias in the presence of Brugada syndrome. *Annals of the Alexandru Ioan Cuza University-Mathematics* 2020; 66(2): 301–322.

[15] Pathmanathan P, Mirams GR, Southern J, Whiteley JP. The significant effect of the choice of ionic current integration method in cardiac electro-physiological simulations. *International Journal for Numerical Methods in Biomedical Engineering* 2011; 27(11): 1751–1770.

[16] Arthurs CJ, Bishop MJ, Kay D. Efficient simulation of cardiac electrical propagation using high order finite elements. *Journal of Computational Physics* 2012; 231(10): 3946–3962.

[17] Vincent KP, Gonzales MJ, Gillette AK, et al. High-order finite element methods for cardiac monodomain simulations. *Frontiers in Physiology* 2015; 6: 217. doi: 10.3389/fphys.2015.00217

[18] Patelli AS, Dedè L, Lassila T, Bartezzaghi A, Quarteroni A. Isogeometric approximation of cardiac electrophysiology models on surfaces: An accuracy study with application to the human left atrium. *Computer Methods in Applied Mechanics and Engineering* 2017; 317: 248–273.

[19] Heidenreich EA, Ferrero JM, Doblaré M, Rodríguez JF. Adaptive macro finite elements for the numerical solution of monodomain equations in cardiac electrophysiology. *Annals of Biomedical Engineering* 2010; 38(7): 2331–2345.

[20] Hoermann JM, Bertoglio C, Kronbichler M, Pfaller MR, Chabiniok R, Wall WA. An adaptive hybridizable discontinuous Galerkin approach for cardiac electrophysiology. *International Journal for Numerical Methods in Biomedical Engineering* 2018; 34(5): e2959.

[21] Hurtado DE, Rojas G. Non-conforming finite-element formulation for cardiac electrophysiology: an effective approach to reduce the computation time of heart simulations without compromising accuracy. *Computational Mechanics* 2018; 61(4): 485–497.

[22] Beeler GW, Reuter H. Reconstruction of the action potential of ventricular myocardial fibres. *The Journal of Physiology* 1977; 268(1): 177–210.

[23] Baumgarten N, Wieners C. The parallel finite element system M++ with integrated multilevel preconditioning and multilevel Monte Carlo methods. *Comput. Math. Appl.* 2021; 81: 391–406. doi: 10.1016/j.camwa.2020.03.004

[24] Vigmond E, Dos Santos RW, Prassl A, Deo M, Plank G. Solvers for the cardiac bidomain equations. *Progress in Biophysics and Molecular Biology* 2008; 96(1-3): 3–18.

[25] Bendahmane M, Karlsen KH. Analysis of a class of degenerate reaction-diffusion systems and the bidomain model of cardiac tissue. *Networks and Heterogeneous Media* 2006; 1(1): 185–218. doi: 10.3934/nhm.2006.1.185

[26] Bourgault Y, Coudiere Y, Pierre C. Existence and uniqueness of the solution for the bidomain model used in cardiac electrophysiology. *Nonlinear Analysis: Real World Applications* 2009; 10(1): 458–482.

[27] Aliev RR, Panfilov AV. A simple two-variable model of cardiac excitation. *Chaos, Solitons & Fractals* 1996; 7(3): 293–301.

[28] Rogers JM, McCulloch AD. A collocation-Galerkin finite element model of cardiac action potential propagation. *IEEE Transactions on Biomedical Engineering* 1994; 41(8): 743–757.

[29] Veneroni M. Reaction–diffusion systems for the macroscopic bidomain model of the cardiac electric field. *Nonlinear Analysis: Real World Applications* 2009; 10(2): 849–868.

[30] Luo Ch, Rudy Y. A model of the ventricular cardiac action potential. Depolarization, repolarization, and their interaction. *Circulation research* 1991; 68(6): 1501–1526.

[31] Morris C, Lecar H. Voltage oscillations in the barnacle giant muscle fiber. *Biophysical Journal* 1981; 35(1): 193–213.

[32] Pargaei M, Kumar BR. On the existence–uniqueness and computation of solution of a class of cardiac electric activity models. *International Journal of Advances in Engineering Sciences and Applied Mathematics* 2019; 11(3): 198–216.

[33] Plank G, Loewe A, Neic A, et al. The openCARP Simulation Environment for Cardiac Electrophysiology. *Computer Methods and Programs in Biomedicine* 2021; 208: 106223. doi: 10.1016/j.cmpb.2021.106223

[34] Lindner L. CardMech framework of M++. *https://git.scc.kit.edu/mpp/cardmech/-/tree/1.0.2*.

[35] Hundsdorfer W, Verwer J. *Numerical solution of time-dependent advection-diffusion-reaction equations*. 33 of *Springer Series in Computational Mathematics*. Springer-Verlag, Berlin . 2003

[36] Hansen E, Ostermann A. Dimension splitting for quasilinear parabolic equations. *IMA J. Numer. Anal.* 2010; 30(3): 857–869. doi: 10.1093/imanum/drn078

[37] Hansen E, Ostermann A. High-order splitting schemes for semilinear evolution equations. *BIT* 2016; 56(4): 1303–1316. doi: 10.1007/s10543-016-0604-2

[38] Einkemmer L, Ostermann A. Overcoming order reduction in diffusion-reaction splitting. Part 2: Oblique boundary conditions. *SIAM J. Sci. Comput.* 2016; 38(6): A3741–A3757. doi: 10.1137/16M1056250

[39] Descombes S. Convergence of a splitting method of high order for reaction-diffusion systems. *Math. Comp.* 2001; 70(236): 1481–1501. doi: 10.1090/S0025-5718-00-01277-1

[40] Altmann R, Ostermann A. Splitting methods for constrained diffusion–reaction systems. *Comput. Math. Appl.* 2017; 74(5): 962–976. doi: 10.1016/j.camwa.2017.02.044

[41] Karlsen KH, Risebro NH. Corrected operator splitting for nonlinear parabolic equations. *SIAM J. Numer. Anal.* 2000; 37(3): 980–1003. doi: 10.1137/S0036142997320978

[42] Descombes S, Ribot M. Convergence of the Peaceman-Rachford approximation for reaction-diffusion systems. *Numer. Math.* 2003; 95(3): 503–525. doi: 10.1007/s00211-002-0434-9

[43] Hansen E, Henningsson E. A convergence analysis of the Peaceman-Rachford scheme for semilinear evolution equations. *SIAM J. Numer. Anal.* 2013; 51(4): 1900–1910. doi: 10.1137/120890570

[44] Gander W, Gander MJ, Kwok F. *Scientific computing – An introduction using Maple and MATLAB*. 11. Springer Science & Business . 2014.

[45] Bayer JD, Blake RC, Plank G, Trayanova NA. A novel rule-based algorithm for assigning myocardial fiber orientation to computational heart models. *Annals of Biomedical Engineering* 2012; 40(10): 2243–2254.

[46] Schuler S. KIT-IBT/LDRB_Fibers. 2021. doi: 10.5281/zenodo.4606575

[47] Lombaert H, Peyrat JM, Croisille P, et al. Human Atlas of the Cardiac Fiber Architecture: Study on a Healthy Population. *IEEE Transactions on Medical Imaging* 2012; 31(7): 1436–1447. doi: 10.1109/TMI.2012.2192743

[48] Kahlmann W, Poremba E, Potyagaylo D, Dössel O, Loewe A. Modelling of patient-specific Purkinje activation based on measured ECGs. *Current Directions in Biomedical Engineering* 2017; 3(2): 171–174.

[49] Gerach T, Schuler S, Fröhlich J, et al. Electro-mechanical whole-heart digital twins: A fully coupled multi-physics approach. *Mathematics* 2021; 9(11): 1247. doi: 10.3390/math9111247

[50] ten Tusscher KH, Panfilov AV. Alternans and spiral breakup in a human ventricular tissue model. *American Journal of Physiology-Heart and Circulatory Physiology* 2006; 291(3): H1088-H1100. doi: 10.1152/ajpheart.00109.2006

[51] O'Hara T, Virág L, Varró A, Rudy Y. Simulation of the undiseased human cardiac ventricular action potential: model formulation and experimental validation. *PLoS Computational Biology* 2011; 7(5): e1002061.

[52] Courtemanche M, Ramirez RJ, Nattel S. Ionic mechanisms underlying human atrial action potential properties: insights from a mathematical model. *American Journal of Physiology-Heart and Circulatory Physiology* 1998; 275(1): H301–H321.

APPENDIX

A THE BEELER–REUTER CELL MODEL

The Beeler–Reuter cell model [22] is defined by the transmembrane voltage v, the intracellular ion concentration of calcium c, and six gating mechanisms $\mathbf{w} = (w_1, \dots, w_6) = (d, f, m, h, j, x_1)$. The total ionic current $I_{\text{ion}}(v, c, \mathbf{w})$ is the sum of the two inward currents

$$I_s(v, c, d, f) = g_s d f (v - E_s(c)), \qquad I_{\text{Na}}(v, m, h, j) = (g_{\text{Na}} m^3 h j + g_{\text{NaC}})(v - E_{\text{Na}}),$$

and the two outward currents

$$I_{x_1}(v, x_1) = x_1 \frac{0.8\big(\exp(0.04(v + 77)) - 1\big)}{\exp(0.04(v + 35))}, \qquad I_{\text{K}}(v) = \frac{1.4\big(\exp(0.04(v + 85)) - 1\big)}{\exp(0.08(v + 53)) + \exp(0.04(v + 53))} + \frac{0.07(v + 23)}{1 - \exp(-0.04(v + 23))},$$

with the reversal potential $E_s(c) = -82.3 - 13.0287 \log(c)$ and $E_{\text{Na}} = 50\,\text{mV}$. Corresponding to [22] the constants are set to

$$g_{\text{Na}} = 4\,\text{mS/cm}^2, \quad g_{\text{NaC}} = 0.003\,\text{mS/cm}^2, \quad g_s = 0.09\,\text{mS/cm}^2.$$

The opening and closing rates $\alpha_k(v)$ and $\beta_k(v)$ in (5) are defined by

$$\alpha_k(v) = \frac{C_{1,k} \exp(C_{2,k}(v + C_{3,k})) + C_{4,k}(v + C_{5,k})}{\exp(C_{6,k}(v + C_{3,k})) + C_{7,k}}, \qquad \beta_k(v) = \frac{C_{1,k} \exp(C_{2,k}(v + C_{3,k})) + C_{4,k}(v + C_{5,k})}{\exp(C_{6,k}(v + C_{3,k})) + C_{7,k}}$$

depending on different parameters $C_{1,k}, \dots, C_{7,k} \geq 0$ for $k = 1, \dots, 6$, cf. Tab. A1.

The potentials are given in mV, the calcium concentration in mol/l and the gating variables are dimensionless. The initial values at $t = 0$ are constant in space and set to

$$v^0 = -84.57\,\text{mV}, \qquad \text{Ca}^0 = 0.0000002\,\frac{\text{mol}}{\text{l}}, \qquad \mathbf{w}^0 = \big(0.002980, 1.0, 0.9877, 0.975, 0.011, 0.00565\big).$$

In G_c from (6) the constants are defined as $w_c = 0.07$ and $\alpha_c = 10^{-7}$. As the gating variables model the status of a gate they switch very fast between zero and one and adopt only values in $[0, 1]$. As c models the calcium concentration in a cardiac cell it is always positive and during one action potential it has values between $[2 \cdot 10^{-7}, 6 \cdot 10^{-6}]$ mol/l. The physiological range of the transmembrane voltage v is in $[-90, 20]$ mV.

TABLE A1 Constants to define α_y and β_y for every gate with equation (5).

	$C_{1,k}$	$C_{2,k}$	$C_{3,k}$	$C_{4,k}$	$C_{5,k}$	$C_{6,k}$	$C_{7,k}$
$\alpha_m \equiv \alpha_3$	0	0	47	-1	47	-0.1	-1
$\beta_m \equiv \beta_3$	40	-0.056	72	0	0	0	0
$\alpha_h \equiv \alpha_4$	0.126	-0.25	77	0	0	0	0
$\beta_h \equiv \beta_4$	1.7	0	22.5	0	0	-0.082	1
$\alpha_j \equiv \alpha_5$	0.055	-0.25	78	0	0	-0.2	1
$\beta_j \equiv \beta_5$	0.3	0	32	0	0	-0.1	1
$\alpha_d \equiv \alpha_1$	0.095	-0.01	-5	0	0	-0.072	1
$\beta_d \equiv \beta_1$	0.07	-0.017	44	0	0	0.05	1
$\alpha_f \equiv \alpha_2$	0.012	-0.008	28	0	0	0.15	1
$\beta_f \equiv \beta_2$	0.0065	-0.02	30	0	0	-0.2	1
$\alpha_{x_1} \equiv \alpha_6$	0.0005	0.083	50	0	0	0.057	1
$\beta_{x_1} \equiv \beta_6$	0.0013	-0.06	20	0	0	-0.04	1
	$\frac{1}{\text{ms}}$	$\frac{1}{\text{ms}}$	$\frac{1}{\text{mV}}$	mV	$\frac{1}{\text{mV} \cdot \text{ms}}$	mV	$\frac{1}{\text{mV}}$	-

B NUMERICAL SETUP

B.1 Parameters and constants for the numerical simulations

The domain $\overline{\Omega}$ is measured in mm. The surface-to-volume-ratio is given by $\chi = 140\,\mathrm{mm}^{-1}$, the membrane capacitance is set to $C_\mathrm{m} = 0.01 \cdot 10^{-6}\ \mathrm{F/mm}^2$, and the anisotropic conductivity in (16) is defined by the parameters

$$D_\mathrm{l} = 0.0001334177215\ \mathrm{Smm}^{-1}, \quad D_\mathrm{t} = 0.00001760617761\ \mathrm{Smm}^{-1}.$$

A standard choice for the constants of the external current is the amplitude $a(\mathbf{x}) = 20\,\mu\mathrm{A/cm}^2$ for all $\mathbf{x} \in \overline{\Omega}_\mathrm{stim}$, the scaling factor $s_\mathrm{ext} = 4$, the start time $t_{\mathrm{beg},i} = 0.0$ and $\tau_j = 0.002\,\mathrm{s}$ for all $i = 1, \ldots, n_\mathrm{stim}$. In Fig. B1 the dependence of the time-continuous version of I_ext on the scaling factor s_ext is plotted at one stimulation point for fixed amplitude and duration.
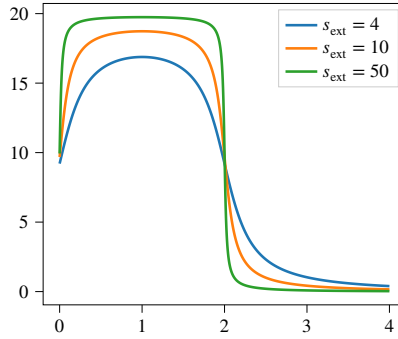

FIGURE B1 Smoothed external stimulus for different s_ext with fixed $a = 20$, $t_\mathrm{beg} = 0$, $\tau = 2$.
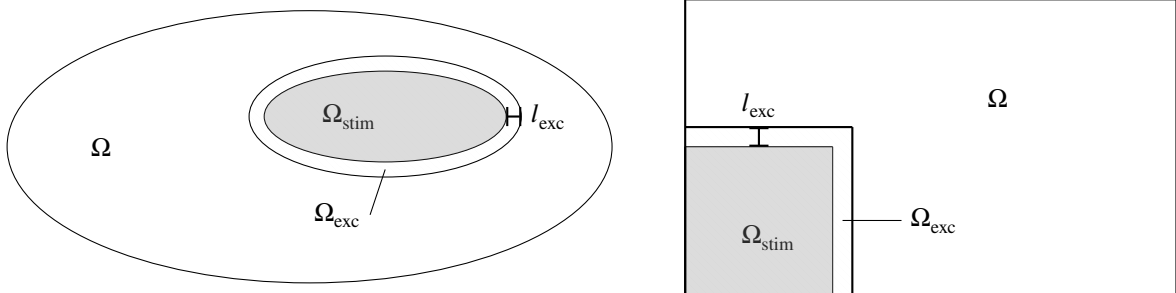

FIGURE B2 Examples to illustrate the set $\overline{\Omega}_\mathrm{exc}$.

TABLE B2 Evaluation points in the truncated ellipsoid, cf. Fig. 1 and Fig. 3.

$\mathbf{z}_1 = (\,0.0, 0.0\,, -17.0\,)$	grid point at apex endocardial excited
$\mathbf{z}_2 = (0.0, 0.0\,, -20.0)$	grid point at apex epicardial
$\mathbf{z}_3 = (0.88, 3.28, -16.95\,)$	grid point inner wall middle of ellipsoid
$\mathbf{z}_4 = (0.2, 0.2, -17.4\,)$	besides grid next to $\mathbf{z}_1$
$\mathbf{z}_5 = (\,0.1, 0.1, -19.8)$	besides grid next to $\mathbf{z}_2$
$\mathbf{z}_6 = (\,-0.98, -3.3, -16.2)$	besides grid next to $\mathbf{z}_3$
$\mathbf{z}_7 = (-1.6, 4.5, -15.8\,)$	besides grid in wall, opposite(y-direction) of $\mathbf{z}_6$

$\mathbf{x}_1 = (-2.571, 0.0, -15.811)$	myocardial wall
$\mathbf{y}_1 = (-5.617, 0.0, -10.105)$	
$\mathbf{x}_2 = (0.0, 5.166, -14.656)$	inner surface
$\mathbf{y}_2 = (0.0, 6.971, -10.556)$	